Journal of Materials Chemistry A

PAPER

View Article Online
View Journal | View Issue

Cite this: J. Mater. Chem. A, 2018, 6, 15738

Reduced expansion and improved full-cell cycling of a SnO_x#C embedded structure for lithium-ion batteries†

Lie Yang,‡[a] Liu-Yang Sun,‡[a] Rong-Rong Zhang,[a] Ya-Wen Xu,[a] Xiao-Hui Ning,*[a] Yuan-Bin Qin,[a] R. Lakshmi Narayan,[b] Ju Li*[c] and Zhi-Wei Shan[a]

SnO_x exhibits a much larger theoretical capacity compared to graphite as an anode material in lithium-ion batteries (LIBs). However, the cycling stability and initial coulombic efficiency (ICE) of SnO_x based electrodes need to be improved. In this study, by coating carbon on a dried SnO_x electrode film using one-step chemical vapor deposition, a SnO_x#C composite is obtained, wherein ~70 nm sized SnO_x nanoparticles are uniformly dispersed and embedded in a carbon matrix. Owing to its relatively small electrochemical surface area and mechanical robustness, the ICE is largely improved from ~40% to >65%. Besides, a Li-matched full cell with 36% excess $LiCoO_2$ cathode material can run stably for more than 100 cycles at 0.1 A g^{-1}, delivering a gravimetric and a volumetric capacity of 456 mA h g^{-1} and 644 mA h cm^{-3}, respectively, which are superior to graphite. The lithiation/delithiation process of SnO_x#C observed using an *in situ* transmission electron microscope technique reveals that the embedded structure expands by only ~5%. Besides, the thickness increment of the electrode film after 100 cycles is measured to be 32%, which is much smaller than the acceptable 50% in the LIB industry, illustrating the good stability of the solid-electrolyte interphase (SEI) skeleton.

Received 23rd May 2018
Accepted 19th July 2018

DOI: 10.1039/c8ta04822c

rsc.li/materials-a

Introduction

Lithium-ion batteries (LIBs) are widely employed in 3C (computer, communication and consumer electronics) products and electric vehicles.[1–4] In both product categories, there is a persistent need to enhance the gravimetric as well as the volumetric energy density of batteries. Tin oxide (SnO_x) exhibits a larger theoretical capacity of ~784 mA h g^{-1} (ref. 5) compared to that of the commercially used graphite based anode (372 mA h g^{-1}). Furthermore, its ideal density (6.95 g cm^{-3}) is triple that of graphite (2.2 g cm^{-3}), making its theoretical volumetric capacity ~6× that of graphite.[6] However, SnO_x suffers from severe capacity fading and poor coulombic efficiency (CE) during cyclic lithiation/delithiation.[7,8] Capacity fading, in the case of tin oxide, is an outcome of the large volumetric change (~250%)[9,10] the material experiences during cycling, which reduces battery performance in the following three ways:[11,12] (a) the active materials crack or pulverize, and lose electrical contact with the current collector; (b) the electrode film loses its compactness, allowing some active material clusters to drift away from the current collector and subsequently become inactive or "dead"; (c) the outer solid-electrolyte interphase (SEI)[13] layer breaks and exposes fresh surfaces of the active materials to the electrolyte. These fresh surfaces participate in unwanted side reactions with the electrolyte, causing dry-out, and further deteriorate the performance of the electrode.

In terms of both structural stability and rate performance, nanometer-sized SnO_x is much better than its bulk counterparts.[14] This is because size reduction of SnO_x improves its strain tolerance[15] and also facilitates faster reaction rates – the latter owing to the significantly reduced solid state diffusion distances. However, some new issues with using nanomaterials need to be addressed. For instance, these particles tend to agglomerate to reduce surface energy.[16,17] Also, more active surfaces are exposed to the electrolyte. Subsequently, an excess coat of unwanted irreversible SEI layers forms over the nanoparticles, resulting in relatively low initial coulombic efficiency (ICE).[18]

In an endeavor to alleviate the problems associated with agglomeration and SEI formation, a novel embedding design, illustrated in Fig. 1a, was proposed. In this design, active SnO_x nanoparticles are embedded homogeneously in a lithium-ion

[a]Center for Advancing Materials Performance from the Nanoscale (CAMP-Nano), State Key Laboratory for Mechanical Behavior of Materials, Xi'an Jiaotong University, Xi'an, Shaanxi 710049, P. R. China. E-mail: xiaohuining@mail.xjtu.edu.cn

[b]Department of Materials Science and Engineering, Carnegie Mellon University, Pittsburgh, Pennsylvania 15213, USA

[c]Department of Nuclear Science and Engineering, Department of Materials Science and Engineering, Massachusetts Institute of Technology, Cambridge, Massachusetts 02139, USA. E-mail: liju@mit.edu

† Electronic supplementary information (ESI) available. See DOI: 10.1039/c8ta04822c

‡ These authors contributed equally to this work.

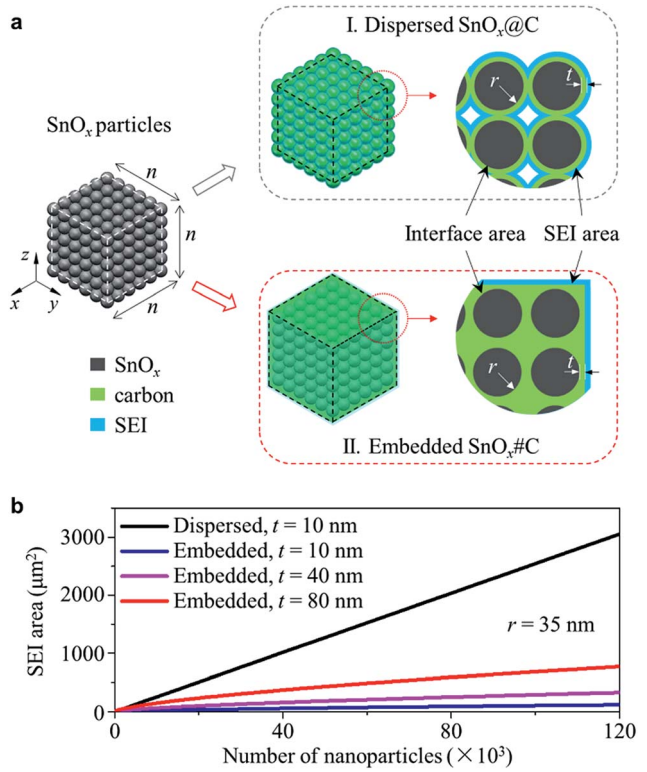

Fig. 1 (a) Schematic illustration of the structures of (I) dispersed and (II) embedded SnO_x/C composites; (b) calculated SEI area of dispersed and embedded SnO_x/C piles (SnO_x: $r = 35$ nm) based on the model in (a). The detailed calculation method is described in Note S1 in the ESI.†

permeable matrix such as carbon. Such a structure separates the particles from each other to minimize their agglomeration. Compared to a general SnO_x@C dispersed structure, where carbon is coated on the surface of each individual particle, a SnO_x#C embedded structure prevents the electrolyte from completely flooding the active nanoparticles. Therefore, the surface area in contact with the electrolyte (SEI area) for embedded SnO_x#C is only about one third of that for dispersed SnO_x@C (see Fig. 1b), which means greatly reduced formation of the SEI layer. Moreover, an embedded structure also circumvents the previously mentioned phenomenon of particle drifting as the enveloping matrix ensures perpetual electrical contact between particles and the current collector in multiple lithiation/delithiation cycles. Note that since the interface area between the embedded active particles and the matrix remains as high as that of the dispersed particles, a high solid-state diffusion rate can be maintained if the thickness and ionic conductivity of the matrix are fine tuned. Up until now, embedded structures such as pitaya-like Sn/C nanocomposites,[19,20] pomegranate-inspired Si@C,[21] Sn/SnO_x nanoparticles encapsulated in carbon microfibers,[22,23] and Sn@SnO_x/C nanocomposites[24] have been prepared using an aerosol spray pyrolysis method, a bottom-up microemulsion approach, electrospinning techniques and oxygen plasma-assisted milling. For alloy-type high-capacity anode materials, these embedded structures exhibit stable capacities and highly impressive rate capabilities. Nevertheless, the above mentioned strategies to prepare embedded structures have certain disadvantages. For instance, pitaya-like Sn/C nanocomposites yield a low mass fraction of active particles; the synthesis technique of pomegranate-inspired Sn@C structures is, in itself, a complex multi-step process. Other synthesis techniques such as electrospinning are too cost intensive. Hence, a facile, cheap, and high yield method to synthesize high performance embedded anode materials is desirable.

In this study, we propose one such simplified technique, wherein carbon is directly deposited on the electrode to produce SnO_x#C embedded structures. This method was originally conceived while resolving the shortcomings of the commonly used slurry pasting method of electrode preparation. The main problem associated with this method, which is unstable electrical contact between active particles, is further exacerbated by the use of active materials that experience expansion and contraction during lithiation/delithiation cycles (loose particles getting insulated or drifting away from collector).[25] Furthermore, poly(vinylidene fluoride) (PVDF), the commonly used binder in this process, has poor electrical conductivity.[26] However, directly coating carbon on the electrode not only produces a SnO_x#C embedded structure that facilitates better contact and structural stability but also turns insulating PVDF polymers into conductive carbon products. This method is easy to implement and utilizes a minimal number of reagents, *i.e.* C_2H_2 gas and high-yielding SnO_x particles, both of which are relatively inexpensive. The obtained SnO_x#C embedded structure exhibits high specific capacity (>1000 mA h g^{-1} at 0.2 A g^{-1} after 150 cycles), excellent rate capabilities, and stable full-cell performance over 100 cycles.

Experimental

Sample preparation

Partially reduced tin oxide (SnO_x) was synthesized by reacting SnO_2 with H_2. For this, the powder of chestnut-like SnO_2 – synthesized by methods reported previously[27] – was placed in an alumina crucible and then placed inside a tube furnace. The tube was then heated to 450 °C, at a rate of 10 °C min^{-1}, and was held at this temperature for 30 minutes. A gas mixture consisting of Ar (285 sccm) and H_2 (15 sccm) was injected into the furnace under ambient pressure. After the tube was cooled down to room temperature, SnO_x was obtained.

The electrodes were prepared by mixing SnO_x, super-P carbon black (AR, Sigma Aldrich), and PVDF (AR, Aladdin) with a mass ratio of 8 : 1 : 1 in *N*-methyl-2-pyrrolidone (NMP, AR, Aladdin) solvent. After stirring this mixture for 24 h, the slurry was pasted onto a pure copper foil and dried at 80 °C for 24 h. The mass loading was 1 mg cm^{-2}.

To coat the dried electrode film with carbon, a chemical vapor deposition (CVD) method, with acetylene as the carbon source, was employed. The electrode was placed in a tube furnace and heated to 700 °C at a rate of 15 °C min^{-1}, and held at this temperature for 10 minutes. After this, the furnace was cooled to room temperature under the protection of Ar gas flow (300 sccm). In the heating process, C_2H_2 (30 sccm) gas was

introduced into the chamber at 600 °C. Following this, the C_2H_2 gas supply was cut off when the temperature dropped to 550 °C. Finally, SnO_x#C embedded composites were obtained.

Characterization of the samples

The morphologies of the prepared samples were characterized using scanning electron microscopy (SEM, Hitachi SU6600). A high resolution transmission electron microscope (TEM, JEOL 2100F, 200 kV) equipped with an energy-dispersive X-ray spectrometer (EDS) was used to investigate the inner structure and chemical composition of the products. The crystal structures of the samples were examined using X-ray diffraction (XRD, PANalytical X'pert Pro, Cu: 40 kV, 40 mA).

Electrochemical measurements

The obtained SnO_x#C electrode was tested using CR2032-type coin cells. For half-cell measurements, pure lithium metal foil was used as the reference and the counter electrode; 1 M $LiPF_6$ in an ethylene carbonate (EC)–dimethyl carbonate (DMC)–ethyl methyl carbonate (EMC) (1 : 1 : 1, vol) solution, with 5.0% fluoroethylene carbonate (FEC), was used as the electrolyte. Inside an Ar-filled glove box (MBraun, Unilab), the cell was assembled while maintaining the moisture and oxygen concentrations below 0.1 ppm. Galvanostatic charge–discharge performance was measured using a battery tester (BST8-MA, MTI) at various current densities between 0.005 and 2.5 V or 0.005 and 1.2 V. Cyclic voltammetry (CV) measurements were conducted on a CHI 660E electrochemical workstation (Shanghai Chenhua) at a scan rate of 0.5 mV s^{-1} and within a voltage range of 0–2.5 V. For the full-cell test, $LiCoO_2$ is used as the cathode. It is prepared by punching the commercial electrode plate into discs with a diameter of 12 mm. The matched SnO_x#C/$LiCoO_2$ full cells were evaluated by galvanostatic cycling in a coin cell at 3.0–3.8 V. To calculate the specific capacity values, the total weight of SnO_x and the coated carbon was used.

In situ TEM observation

The *in situ* TEM characterization was carried out using an environmental transmission electron microscope (ETEM, Hitachi H9500, 300 kV) using the PI 95H1H holder (Hysitron). An all-solid nanobattery was assembled. The SnO_x#C embedded composite was attached to an aluminum plate with conductive silver epoxy and used as the working electrode. Li metal loaded on a tungsten tip was used as the counter electrode. The naturally formed Li_2O layer on the surface of the Li metal was used as the solid electrolyte. A bias potential of −10.0 V was applied to the SnO_x#C anode to initiate the lithiation. The delithiation occurs when the applied bias potential is reversed. The morphology and size change during lithiation/delithiation are observed and recorded for further analysis.

Results and discussion

Morphological and structural characterization

Using C_2H_2 as the source, carbon is coated on the electrode *via* chemical vapor deposition. At the corresponding operating temperature of 700 °C, which is much higher than the melting point of tin (232 °C), the active material – SnO_x particles – tends to agglomerate. Hence, the SnO_x particles should be dispersed and separated before initiating the carbon-coating process. Also, in order to facilitate smoother diffusion of ions, it is crucial to limit the thickness of the coated carbon layer. This can only be achieved by minimizing the size of SnO_x particles to such an extent that only a very thin layer of carbon is necessary to ensure structural robustness. To obtain small sized, isolated SnO_x particles, we thermally reduced chestnut-like SnO_2 particles (obtained *via* hydrothermal oxidation of Sn particles, as reported in our previous work[21]) in hydrogen gas. As shown in Fig. 2a, S1a and b,† instead of inheriting the hollow, chestnut-like configuration of SnO_2, the morphology of the SnO_x product evolves into a unique mass of spherical and faceted nanoparticles dispersed within a porous network (indicated by a black arrow in Fig. S1b†). The X-Ray Diffraction (XRD) curve of SnO_x, displayed in Fig. 2c, contains peaks corresponding to both Sn (PDF#04-0673) and SnO_2 (PDF#41-1445). Furthermore, EDS mapping of the whole embedded structure (see Fig. S1c†) confirms the presence of SnO_x and carbon in the nanoparticles and porous network, respectively. In the context of the high temperature carbon-coating process that will be described next, the presence of the enveloping porous carbon skeleton would prevent individual SnO_x particles from agglomerating. Also, the average diameter of the SnO_x particles, measured to be approximately 88 nm (see Fig. S2a†), is optimal for tolerating strains originating from subsequent lithiation/delithiation-induced volume changes.[17] Note that each dispersed nanometer-sized SnO_x particle evolves from a single carbon coated SnO_2 nanosheet on the chestnut-like SnO_2 particle, as shown in Fig. S3.†

Next, these SnO_x particles were mixed with super-P carbon black and PVDF binder with a mass ratio of 8 : 1 : 1 in NMP solvent to prepare the electrode. As shown in Fig. 2b, prior to coating carbon, SnO_x particles (denoted by a white arrow) and the super-P carbon black (black arrow) are uniformly dispersed and bound by PVDF (yellow arrow) polymers in the electrode film. Thereafter, during chemical vapor deposition, acetylene and PVDF decompose into carbon products, which cover the surface of the SnO_x particles and merge with the pre-existing super-P carbon black to form a continuous carbon matrix. A schematic illustration of this process is shown in Fig. 2d. The obtained carbon coated electrode (SnO_x#C) (see Fig. 2e) has a smoother appearance than the pristine electrode displayed in Fig. 2b. This difference in appearance manifests the substitution of PVDF, which decomposes at high temperatures (see Fig. S4†), leaving behind a continuous 3D host of carbon. A few rod-like structures also form due to the unavoidable partial agglomeration of Sn particles at high temperatures. Regardless, the SnO_x#C electrode exhibits the same characteristic peaks in the XRD curve as those exhibited by SnO_x particles (see Fig. 2c) – implying that the high temperature coating procedure successfully retains the original constituents. However, an increase in the relative intensity of Sn implies that SnO_2 is further reduced by carbon during the heat treatment. Also, it should be mentioned that the characteristic peaks representing

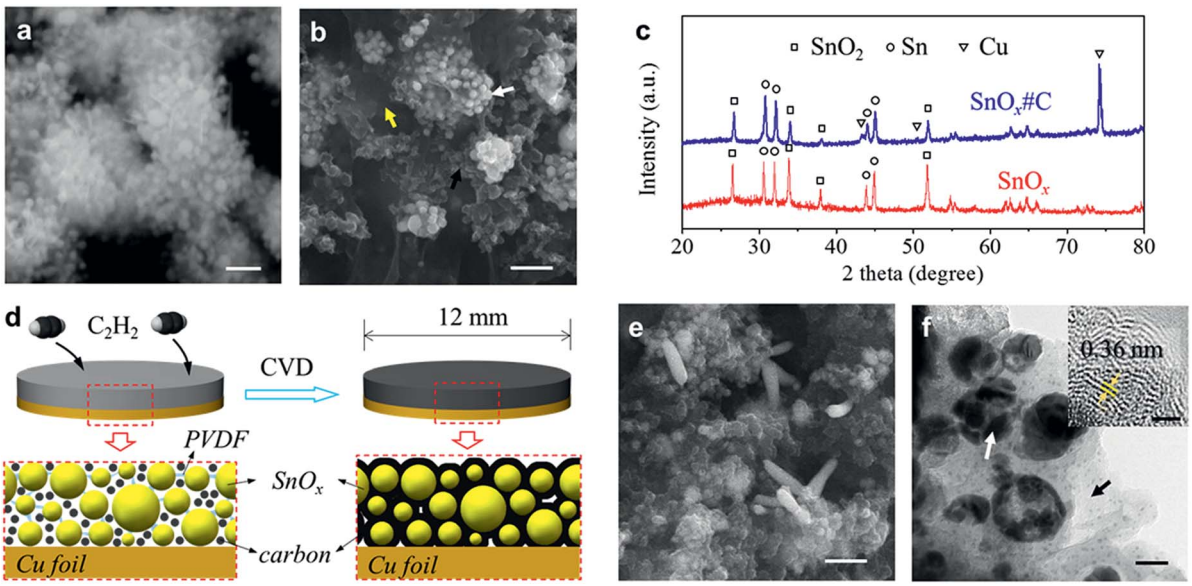

Fig. 2 Morphological and structural characterization of SnO_x and the SnO_x#C composite: (a) SEM image of SnO_x particles, scale bar: 200 nm; (b) SEM image of the dried SnO_x electrode before coating carbon, scale bar: 500 nm; (c) XRD patterns of SnO_x particles and the SnO_x#C electrode; (d) schematic illustration of the carbon-coating process on the electrode film *via* chemical vapor deposition; (e) SEM image of the SnO_x#C electrode after coating carbon, scale bar: 500 nm; (f) TEM image of the SnO_x#C embedded composite, scale bar: 50 nm; the inset shows a high resolution TEM image (HRTEM) of the carbon matrix, scale bar: 2 nm.

Cu (PDF#04-0836) on the XRD curves originate from the Cu foil on which the electrode materials are pasted. As further revealed by the TEM image in Fig. 2f and EDS mapping in Fig. S1d,† SnO_x particles with an average diameter of ~74 nm (indicated by a white arrow in Fig. 2f) were uniformly dispersed inside the 3D continuous carbon host (indicated by a black arrow). Apart from these larger particles, some ~8 nm sized Sn particles, probably resulting from the outward diffusion of elemental tin, were also found to be distributed within the carbon matrix (see Fig. S5a†). In the inset of Fig. 2f, ordered parallel lattice fringes with a spacing of 0.36 nm can be observed in a high resolution TEM image of the carbon matrix. This indicates that the coated carbon matrix is partially graphitized and should possess decent electrical conductivity. It was also noted that the total weight of the electrode film remains nearly unchanged after chemical vapor deposition. Thus, the reduction in the mass of the film from pyrolysis of PVDF is completely balanced by the gain in mass from the deposition of C_2H_2. From this, the mass fraction of the carbon matrix (composed of the deposited carbon, super-P carbon black and other products of PVDF decomposition) in the SnO_x#C composite is determined to be ~20%. In summary, nanometer-sized SnO_x particles embedded in a graphitized carbon matrix were successfully produced *via* a facile, low-cost chemical vapor deposition method.

Electrochemical performance

Half cells with superabundant lithium metal foil as the counter/reference electrode and the SnO_x#C embedded structure as the working electrode are assembled and tested by galvanostatic cycling. The CV curve, obtained at a scan rate of 0.5 mV s^{-1} between 0 and 2.5 V (*vs.* Li/Li^+) is displayed in Fig. S6a.† Cathodic and anodic peaks corresponding to SnO_x appear at 0.25 V, 0.46 V, and 0.6 V, and 0.7 V, 0.8 V, and 0.84 V, respectively.[28] This implies that the cell's capacity is primarily contributed by SnO_x. Moreover, the curves corresponding to the 2nd and 6th cycle have similar peak intensities and almost overlap with each other, thus confirming the highly reversible nature of the electrochemical reactions. The voltage profiles of the SnO_x#C embedded structure measured in the voltage range of 0.005–2.5 V and at a current density of 200 mA g^{-1} are shown in Fig. 3a. The first lithiation and delithiation event delivers a capacity of 1700 mA h g^{-1} and 1120 mA h g^{-1} (calculated w.r.t. the total mass of SnO_x#C), respectively, which corresponds to an ICE of 65.9% in the first cycle. Compared to this, the ICE of SnO_x, without the carbon matrix coating, is only ~40% (see Fig. S7†). In general, such an improvement in the ICE diminishes the need for excess cathode materials in a full-cell assembly. Note that the delithiation capacity in the 1st cycle is much higher than the individual capacities of Sn (992 mA h g^{-1}) and SnO_2 (784 mA h g^{-1}), which suggests that a fraction of Li_2O, maybe owing to its ultra-small size (Fig. S5†),[29–31] can reversibly convert to Li ions. Moreover, the complete overlap of the charging segments in the 1st and 2nd cycle indicates that cycling stability is achieved in the early stages itself. In the 50th and 100th cycle, both the discharge voltage plateaus (0.65 V and 0.4 V) and the charge voltage plateaus (0.6 V, 0.72 V and 0.8 V) become rather smeared out compared to what they were in the 2nd cycle. This appears to be triggered by amorphization of SnO_x.[32] However, these changes are inconsequential in the broader context as the overall capacity remains largely unaffected.

The cycling stability of the SnO_x#C composite in half cells is further examined, as shown in Fig. 3b. It is observed that even

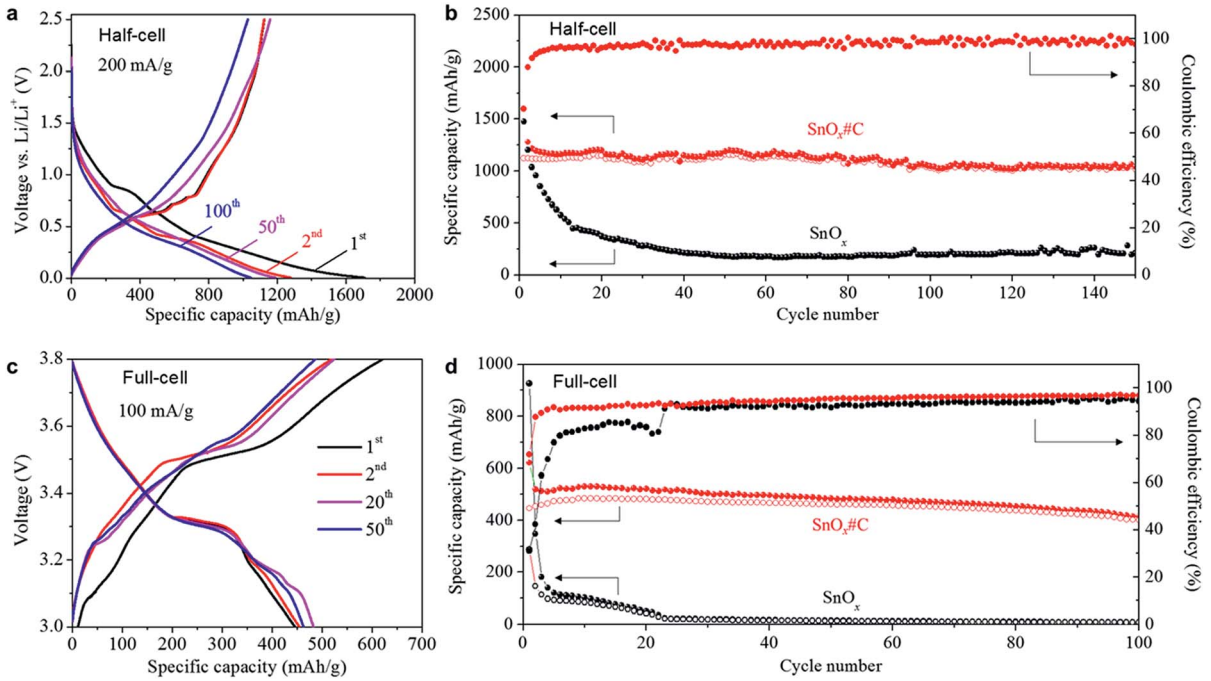

Fig. 3 Electrochemical performance of the SnO_x#C composite. (a) Half-cell charge/discharge voltage profiles of the SnO_x#C composite for the 1st, 2nd, 50th, and 100th cycles at a current density of 200 mA g^{-1}; (b) comparison of the half-cell cycling performance of SnO_x and SnO_x#C at a current density of 200 mA g^{-1} (arrows indicate the reference axes); (c) full-cell charge/discharge voltage profiles of the 1st, 2nd, 20th, and 50th cycle at a current density of 100 mA g^{-1}; (d) comparison of the full-cell cycling performance of SnO_x and SnO_x#C at a current density of 100 mA g^{-1}.

after 150 cycles, the specific capacity is consistently larger than 1040 mA h g^{-1}, at 0.2 A g^{-1}, which corresponds to a capacity retention ratio of 81.3%. To the best of our knowledge, no other SnO_x electrode, hitherto reported in the literature, has a better cycling performance than this[19,20,33–39] (see Fig. S8†). The cycle performance of the SnO_x electrode without the carbon coating is markedly poorer, as its capacity rapidly drops to 358 mA h g^{-1} (lower than that of commercial graphite) after just 21 cycles. Clearly, by developing an embedded structure on the electrode *via* the carbon-coating process, the cycling performance of SnO_x improves significantly. Next, as can be seen in Fig. S6c,† even at lower working potentials (between 0.005 and 1.2 V), the composite exhibits a relatively stable and high capacity of about 700 mA h g^{-1}. It should be mentioned that this is almost twice as high as the theoretical capacity of commercial graphite. Moreover, this composite also exhibits high rate capability. As shown in Fig. S6b and d,† it delivers a capacity of ~625 mA h g^{-1} at 2 A g^{-1} and outperforms the commercial graphite electrode significantly. Additionally, it regains its original capacity when the current density is restored to 0.1 A g^{-1}. We also performed galvanostatic cycling at larger incremental steps of 0.5 A g^{-1} and observed that the capacity hardly changes, thus proving that the composite can also withstand current fluctuations. In fact, at even higher current densities of 1 A g^{-1} and 2 A g^{-1}, SnO_x#C delivers a stable and high capacity of 800 mA h g^{-1} and 500 mA h g^{-1}, respectively, for 160 cycles (see Fig. S6e†). According to the electrochemical impedance spectra (EIS) of SnO_x and SnO_x#C half cells, as shown in Fig. S9 and Table S1,† the charge transfer resistance of SnO_x#C (5.32 Ω) is largely reduced compared with that of SnO_x (61 Ω), probably due to the robust conductive carbon matrix. Besides, the Li ion diffusion coefficient is also obviously improved from 3.43×10^{-17} cm^2 s^{-1} to 2.00×10^{-16} cm^2 s^{-1}. The enhanced transportation of both electrons and lithium ions may contribute to the above excellent rate capabilities.

A half-cell test has certain known limitations. The inexhaustible supply of Li from the superabundant lithium metal counter-electrode (~50 mA h (ref. 40)) will conceal loss-of-recyclable Li effects arising from the formation of SEI films on the anode's surface (more on this later). Thus, to quantify recyclable-Li exhaustion, a full-cell test, utilizing $LiCoO_2$ (capacity of 1.6 mA h, MTI corp., Fig. S10†) as the cathode material, was performed. Since the capacity of the SnO_x#C anode (~1040 mA h g^{-1}) is 1.18 mA h, the $LiCoO_2$ cathode has 36% excess capacity. Fig. 3c displays the charge/discharge profiles of the cell cycled at a current density of 100 mA g^{-1} (based on the weight of SnO_x#C), in the voltage range of 3.0–3.8 V. The first charge and discharge capacities are 621 and 446 mA h g^{-1}, respectively, giving an ICE of 71.8%. A distinct voltage plateau, which appears at 3.3 V in all the discharge curves, persists even after several tens of cycles. Most importantly, the cell retains a stable capacity of more than 400 mA h g^{-1} after 100 cycles, with a capacity retention of 89.7%, as shown in Fig. 3d. At this point it is worth mentioning that although some promising anode materials exhibit excellent gravimetric capacities, their volumetric capacities are usually poorer than that of graphite. This is because, most of these materials, as a consequence of incorporating nano-meter sized

particles, have low tap densities.[41] In comparison, our SnO_x#C embedded composite electrode, with a mass loading of 1.0 mg cm^{-2}, a disc area of 1.13 cm^2, an electrode thickness of 8 μm and an average discharge capacity of 456 mA h g^{-1}, has a volumetric capacity of 644 mA h cm^{-3} (456 mA h g^{-1} × 1.0 mg cm^{-2} × 1.13 cm^2/8 μm), which is higher than that of graphite (550 mA h cm^{-3}). The results obtained thus clearly prove that a full cell incorporating the SnO_x#C composite electrode will run stably for hundreds of cycles and also possess impressive volumetric and gravimetric capacities.

Reduced expansion

Based on the results of the half- and full-cell tests, the strategy to produce an embedded structure of SnO_x#C by coating carbon on the electrode film can be appraised as a novel and effective approach to solve the capacity fading problem of SnO_x. The enhanced capacity stability means that the amount of available active material remains nearly invariant. Hence, it appears that the capacity fading mechanisms (a) and (b) mentioned in the Introduction section of this paper are effectively prevented. To further understand how this was achieved, we opened some half cells that had undergone several charge/discharge cycles. The thickness variations of the electrode film, measured at different stages of cycling, are displayed in Fig. 4a. Note that the SnO_x#C electrode film is about 15% thinner than the SnO_x electrode. This reduction in thickness is caused by the pyrolysis of the loose PVDF binders, followed by densification and contraction of the carbon coating. Thereafter, the SnO_x#C film expands gradually as the cell is charged and discharged. However, the rate of expansion is modest, considering that the film's thickness increases only by 8% between the 27th delithiation and 28th lithiation cycles (see Fig. 4a). Evidently, the 3D continuous carbon skeleton acts a buffer and constrains the inherent tendency of SnO_x materials to expand. As a result, the electrode film only experiences a 32% increase in thickness – from 17.6 μm to 23.3 μm – after 100 cycles (see Fig. 4a). From the point of view of LIB industry requirements,[40] which tolerates up to a 50% increase in thickness, the SnO_x#C film exhibits excellent dimensional stability. For other SnO_x based electrodes, the thickness increases rapidly as SEI layers continuously accumulate over the unstable active surface that is exposed to the electrolyte. The marginal change in the dimensions of our SnO_x#C indicates that the growth of the SEI is successfully restrained by its unique embedded structure. For the sake of comparison, SEM images of the SnO_x and SnO_x#C electrodes are displayed in Fig. S11.† As can be seen in this figure, although both electrodes underwent 100 charge/discharge cycles, the one with the carbon coating has accumulated a lower amount of SEI. Using scanning transmission electron microscopy (STEM), the morphology of the SnO_x#C composite is further characterized. Fig. 4b displays the images of the composite after it underwent 300 charge/discharge cycles. It is apparent that the embedded structure maintains its integrity (compare Fig. 4b and 2f) and remains crack-free even after several hundred cycles. The excellent mechanical endurance of the embedded structure manifests primarily from the use of the ultra-small sized SnO_x particles. Since smaller particles have higher flaw tolerance, they can easily alleviate any internal stresses and strains arising from the lithiation/delithiation process. Moreover, even if the SnO_x particles pulverize during cycling, the surrounding carbon matrix would ensure that the fragmented pieces would remain confined within it and also maintain a good electrical connection with the substrate. This clearly demonstrates the crucial role played by embedded SnO_x structures in mitigating the particle-dispersion mediated capacity fading mechanism. In addition, since both large (~74 nm) and small (~8 nm) SnO_x particles do not agglomerate due to the isolating nature of the carbon matrix, their individual active surfaces always function at maximum efficiency, which further adds to the stability and capacity of the cell. The prominent structural features of the newly-developed SnO_x#C embedded electrode that enhance the rate capability of the cell are identified as follows. First, the porous nature of the electrode film (see Fig. 2e) facilitates ion diffusion and also ensures intimate contact with the electrolyte. Second, ultra-small SnO_x particles ensure shorter solid state diffusion distances. Finally, the persistent contact between SnO_x particles and the conductive carbon matrix promotes smooth electron transportation and ion exchange. All these factors offer a synergistic coupling effect to improve the electrochemical behaviour of electrode materials.

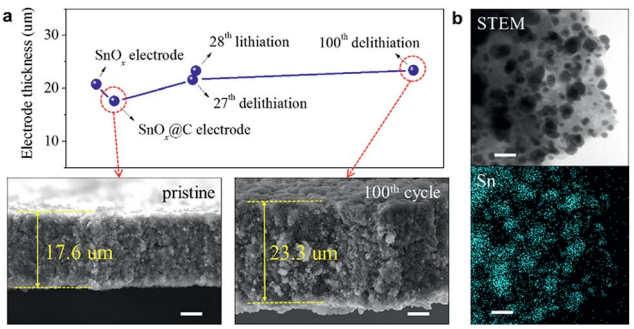

Fig. 4 (a) Variation of the electrode thickness during cycling and corresponding *ex situ* SEM images of the electrode film cross section; scale bar: 5 μm; (b) STEM images of the SnO_x#C composite after ~300 cycles, and corresponding Sn element mapping; scale bar: 100 nm.

As mentioned earlier, the specific surface area of the embedded SnO_x#C composites, which represents the area exposed to the electrolyte, is minimal compared to that of individual SnO_x particles. This ensures that only a limited amount of SEI is present in the former. As a result, the CE of the electrode improves. Additionally, the volume expansion of the SnO_x#C composite during cycling also plays a critical role in the stability of the SEI. As indicated in the former electrode thickness measurement, the volume expansion seems to be accommodated by unfilled voids, which form inside the carbon matrix during the coating process. To confirm this, the real-time structural and morphological evolution of the composite, when it undergoes lithiation and delithiation, is observed with *in situ* TEM. The nano-battery assembly, which employs a lithium metal foil as the counter/reference electrode and the naturally formed Li_2O layer on its surface as the solid

electrolyte, is shown in Fig. 5a. By biasing the SnO_x#C anode with a potential of −10.0 V and +10.0 V, the SnO_x#C composite is lithiated and delithiated, respectively (Fig. 5b). As shown in Fig. 5c and Movie S1,† the SnO_x#C expands when lithiated from 0 s to 55 s, and contracts when delithiated from 55 s to 93 s. To illustrate the expansion more clearly, the outlines of the SnO_x#C composite and a typical embedded SnO_x particle were drawn and are shown in Fig. 5d. It can be seen that, during the lithiation process, the SnO_x particles embedded inside the carbon matrix expand significantly (the red area at 55 s), while the overall expansion of the SnO_x#C composite assembly is negligible (the blue area at 55 s). Moreover, both SnO_x particles and the entire SnO_x#C composite assembly nearly revert to their original states after delithiation at 93 s. Next, the apparent areas of the SnO_x particles and that of the SnO_x#C composite assembly (see Fig. 5c), before and after lithiation, are measured and approximated to the volume of equivalent spheres. As shown in Fig. 5e, the volume change in the former is 90%, which far exceeds the 5% change in the latter. Moreover, the 5% volume change of the SnO_x#C composite is consistent with the 8% change in the thickness of the electrode film (see Fig. 4a). This clearly highlights the role played by the carbon matrix in limiting the volume expansion of the embedded SnO_x particles, which in turn helps maintain the structural integrity of the SEI and promotes overall cell stability.

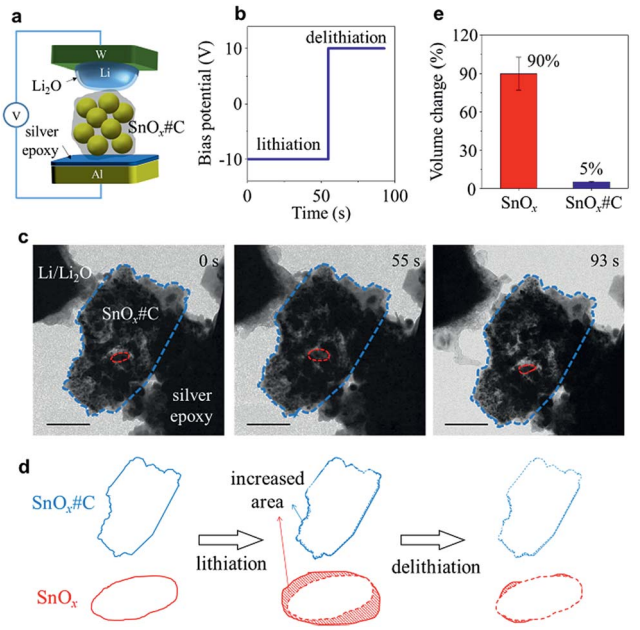

Fig. 5 *In situ* TEM observation of the volume change of SnO_x#C during the lithiation/delithiation process: (a) Schematic illustration of the nanobattery set-up; (b) bias potential applied to the SnO_x#C during the lithiation/delithiation process; (c) still frames extracted from the recorded movie at the pristine state (0 s), lithiated state (55 s) and delithiated state (93 s), scale bar: 500 nm; see Movie S1† for the real-time visualization of the dynamic lithiation process; (d) outlines of SnO_x#C composite assembly and a typical SnO_x particle (corresponding to the dashed areas in (b)) during lithiation/delithiation, exhibiting the change of apparent area. The dashed lines represent the outlines at the pristine state; (e) calculated average volume expansion of individual SnO_x particles and the whole SnO_x#C composite based on the measured apparent areas marked in (c) and (d).

CE analysis of the full cell

The average CE measured in the full-cell test is 94.4%, which is quite low compared to the industry standard CE of >99.9%[42] and also seems to contradict our conclusions regarding the stability of the SnO_x#C anode. Typically, the low CE can occur due to the following three reasons. First, deterioration of the active material occurs, wherein a part of the active material loses electrical contact with the current collector. Subsequently, all lithium stored in these insulated particles are rendered useless, and hence considered dead. Such an event not only reduces the CE but also accelerates capacity fading. The poor electrochemical performance of dispersed SnO_x particles (see Fig. 3d) is attributed to this mechanism. Second, lithium ions absorbed by the anode participate in irreversible side reactions with the electrolyte to form SEI layers. While this will certainly lower the average CE, the measured capacity (mA h g^{-1}), under certain conditions, can remain unaffected. Such conditions are realized if the anode has access to an unlimited supply of Li ions, such as the half-cell tests. Third, trace soluble redox mediators (SRMs),[43] which shuttle between the electrodes, emerge in the electrolyte. SRMs can consume electrons after reacting with the electrode and produce an effect that resembles the self-discharge of the battery (Fig. S12†). However, since their presence has no influence on the quantity of reversible Li ions or the structure of the electrode, they usually won't cause destabilized performance of the half cell or full cell, except for low CE.

The first possibility, involving the deterioration of active materials, can be ruled out as the cause for low CE. This is because the SnO_x#C composite exhibits enhanced cycling stability and there is no evidence to suggest that its active particles have lost contact with the current collector. However, as mentioned earlier, it is difficult to determine which of the other two mechanisms are responsible for lowering the CE during the half-cell test. To reiterate, the intrinsic Li-hosting capacity of the SnO_x#C electrode is limited (~1.18 mA h) while the lithium foil counter electrode in the half cell provides a superabundant source of Li (~50 mA h (ref. 40)). Hence, the half-cell can run stably without Li exhaustion problems for a long time even if SEI layers form continuously on the electrode. But one would not have this luxury in industry with Li-matched full cells.

To identify the dominant mechanism of low CE, irreversible side reaction (SEI) and reversible side reaction (SRM), one can analyze the cycling performance of an approximate full cell. We define a term 'remnant capacity (RC_n)' w.r.t. the cathode as $RC_n \equiv Q_{cathode} - CLC_n$, where n signifies the n^{th} cycle, $Q_{cathode}$ is the amount of Li in the pristine $LiCoO_2$ cathode, CLC_n is defined as $CLC_n = \sum_1^n (Q_{charge,n} - Q_{discharge,n})$, which represents the "capacity loss cumulant", *i.e.* the accumulated loss of lithium ions in the cathode until the n^{th} cycle. For the full cell in Fig. 3d, $Q_{cathode}$ = 1.6 mA h, the RC is calculated and plotted as

a function of cycle number in Fig. 6a. As can be seen from the figure, RC monotonically decreases with increasing number of cycles. From the 1st to the 16th cycle, the capacity of the cathode is consistently larger than that of the SnO_x#C anode (black dots in Fig. 6a). However, at the 17th cycle, the RC equals ~0.54 mA h, which also corresponds to the actual capacity of the anode. If the second mechanism – involving the continuous formation of the SEI on active materials – was indeed dominant, these observations will have the following implications. The presence of SEI layers will prevent reversible utilization of Li ions at the anode. Hence, for the cell to function in a stable manner, the cathode must be capable of supplying an excess amount of Li ions. According to Fig. 6a, the cathode can easily meet this requirement until the 17th cycle as it has higher capacity than the anode. However, beyond the 18th cycle, since the capacity of the anode is higher, the cell capacity should have faded rapidly and become dead by the end of the 32nd cycle. But since Fig. 3d suggests that the full cell is able to perform remarkably well for 100 cycles, the loss in CE cannot be induced by the irreversible utilization of Li.

Therefore, with the actual full-cell performance drastically different from RC prediction in Fig. 6a, the operation of some SRMs in the electrolyte[40,43,44] rather than SEI formation becomes the possible reason that causes the observed low CE. For instance, the SnO_x#C embedded composite contains pyrolysis products of PVDF and C_2H_2. Some of the organic pyrolysis products with functional groups like –C=C–, –C≡C–, and –F, may dissolve in the electrolyte and then either directly act as SRMs or react with the electrolyte to form some other SRMs. To confirm the existence of SRMs, the self-discharge behaviour of SnO_x#C full cells is studied by charging the cells to different constant voltages, where the self-discharge current is defined as the final stabilized current (see Fig. 6b). It can be seen that SnO_x#C full cells exhibit a self-discharge current of ~7.5 μA at 3.8 V, which is close to the calculated hypothetical self-discharge current of 3–5 μA obtained *via* dividing the capacity loss with the charge/discharge time of each cycle (Fig. S13†). Therefore, the self-discharge current attributed to SRMs is proved to be responsible for the low CE of SnO_x#C full cells. Although self-discharge commonly exists in SnO_x#C cells, it won't deteriorate the cells' cycling stability (Fig. 3d) and shelf-life drastically, because the self-discharge current becomes smaller at lower cell voltage. As shown in Fig. S14a,† the self-discharge current decreases from ~8 μA at 3.8 V to almost 0 μA at 3.2 V. Thus, the capacity loss rate, which is determined by the self-discharge current, will continuously decrease and finally become zero with the extension of the static duration. This is further confirmed by the shelf-life test shown in Fig. S14b,† where the slope of discharge voltage curve gets gentler along with increased static duration. After a static duration of 12 hours, the cell voltage remains as high as 3.6 V, which corresponds to a capacity retention of 91.8% and self-discharge current of 5.7 μA, smaller than the CE predicted 8 μA. Altogether, the main implication of the preceding discussion is that low CE does not necessarily imply poor full-cell cycling or short shelf-life. In some cases, it can also be artificially induced by trace SRMs. More future work is still needed to identify the specific SRM and figure out the solution to improve the CE of the full cell.

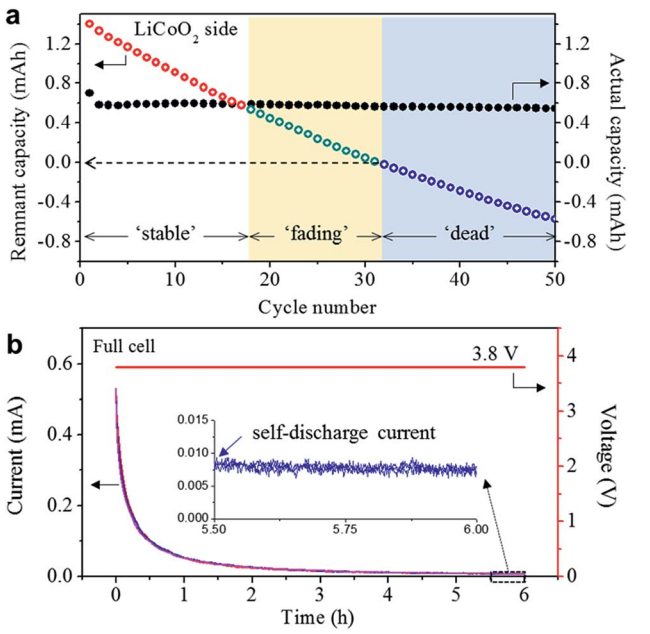

Fig. 6 CE analysis of SnO_x#C full cells: (a) remnant capacity of the $LiCoO_2$ cathode during cyclic lithiation/delithiation; (b) self-discharge current of the full cell measured *via* constant voltage charging.

Conclusions

In summary, we have developed a facile, cost-effective method to prepare a SnO_x#C embedded structure by directly vapor depositing carbon on the electrode film. The embedded active materials do not crack or pulverize as their volume expansion is effectively mitigated. A half-cell assembled with SnO_x#C as the anode exhibits a long cycle life and excellent rate capability. This cell has a stable capacity of ~1040 mA h g^{-1} over 150 cycles at a current density of 0.2 A g^{-1} and also retains a minimum capacity of 500 mA h g^{-1}, after 150 cycles, at a high rate of 2.0 A g^{-1}. In the full-cell test, which employs a $LiCoO_2$ cathode, the cell exhibits cycling stability for over 100 cycles. These results encourage the use of SnO_x#C embedded structures as anodes for high energy density LIBs. In addition to this, this facile method can also be implemented to incorporate other small sized and discretized materials, such as Si nanoparticles, in electrodes.

Conflicts of interest

There are no conflicts of interest to declare.

Acknowledgements

This work was supported by the National Key R&D Program of China (2018YFB0905600, 2017YFB0702001), and the National Natural Science Foundation of China (U1766216, 51401157). The authors acknowledge the International Joint Laboratory for

Micro/Nano Manufacturing and Measurement Technologies for the test service. We thank Dr De-Gang Xie and Ms. Qin-Qin Fu from XJTU for their help in the *in situ* TEM experiment.

Notes and references

1 D. Andre, H. Hain, P. Lamp, F. Maglia and B. Stiaszny, *J. Mater. Chem. A*, 2017, **5**, 17174–17198.
2 Y. Li, J. Yang and J. Song, *Renewable Sustainable Energy Rev.*, 2017, **71**, 645–651.
3 B. Diouf and R. Pode, *Renewable Energy*, 2015, **76**, 375–380.
4 B. Dunn, H. Kamath and J. M. Tarascon, *Science*, 2011, **334**, 928–935.
5 Y. Idota, T. Kubota, A. Matsufuji, Y. Maekawa and T. Miyasaka, *Science*, 1997, **276**, 1395–1397.
6 M. N. Obrovac and V. L. Chevrier, *Chem. Rev.*, 2014, **114**, 11444–11502.
7 S. Ding, J. S. Chen and X. W. Lou, *Adv. Funct. Mater.*, 2011, **21**, 4120–4125.
8 M. S. Park, G. X. Wang, Y. M. Kang, D. Wexler, S. X. Dou and H. K. Liu, *Angew. Chem., Int. Ed.*, 2007, **46**, 750–753.
9 J. Y. Huang, L. Zhong, C. M. Wang, J. P. Sullivan, W. Xu, L. Q. Zhang, S. X. Mao, N. S. Hudak, X. H. Liu, A. Subramanian, H. Fan, L. Qi, A. Kushima and J. Li, *Science*, 2010, **330**, 1515–1520.
10 M. Ebner, F. Marone, M. Stampanoni and V. Wood, *Science*, 2013, **342**, 716–720.
11 H. Wu and Y. Cui, *Nano Today*, 2012, **7**, 414–429.
12 R. Retoux, T. Brousse and D. M. Schleich, *J. Electrochem. Soc.*, 1999, **146**, 2472–2476.
13 J. Y. Cheong, J. H. Chang, H. K. Seo, J. M. Yuk, J. W. Shin, J. Y. Lee and I. D. Kim, *Nano Energy*, 2016, **25**, 154–160.
14 J. S. Chen and X. W. Lou, *Small*, 2013, **9**, 1877–1893.
15 X. H. Liu, L. Zhong, S. Huang, S. X. Mao, T. Zhu and J. Y. Huang, *ACS Nano*, 2012, **6**, 1522.
16 X. L. Wang, M. Feygenson, M. C. Aronson and W.-Q. Han, *J. Phys. Chem. C*, 2010, **114**, 14697–14703.
17 J. Wang, F. Fan, Y. Liu, K. L. Jungjohann, S. W. Lee, S. X. Mao, X. Liu and T. Zhu, *J. Electrochem. Soc.*, 2014, **161**, F3019–F3024.
18 Y. Wan, L. Wang, Y. Chen, X. Xu, Y. Wang, C. Teng, D. Zhou and Z. Chen, *J. Alloys Compd.*, 2018, **740**, 830–835.
19 N. Zhang, Q. Zhao, X. Han, J. Yang and J. Chen, *Nanoscale*, 2014, **6**, 2827–2832.
20 Y. Xu, Q. Liu, Y. Zhu, Y. Liu, A. Langrock, M. R. Zachariah and C. Wang, *Nano Lett.*, 2013, **13**, 470–474.
21 N. Liu, Z. Lu, J. Zhao, M. T. McDowell, H.-W. Lee, W. Zhao and Y. Cui, *Nat. Nanotechnol.*, 2014, **9**, 187–192.
22 Y. Yu, L. Gu, C. Zhu, P. A. van Aken and J. Maier, *J. Am. Chem. Soc.*, 2009, **131**, 15984–15985.
23 B. Zhang, J. Huang and J. K. Kim, *Adv. Funct. Mater.*, 2015, **25**, 5222–5228.
24 H. Liu, R. Hu, W. Sun, M. Zeng, J. Liu, L. Yang and M. Zhu, *J. Power Sources*, 2013, **242**, 114–121.
25 W. J. Zhang, *J. Power Sources*, 2011, **196**, 13–24.
26 H. P. Xu and Z. M. Dang, *Chem. Phys. Lett.*, 2007, **438**, 196–202.
27 L. Yang, T. Dai, Y. Wang, D. Xie, R. L. Narayan, J. Li and X. Ning, *Nano Energy*, 2016, **30**, 885–891.
28 N. Mohri, B. Oschmann, N. Laszczynski, F. Mueller, J. von Zamory, M. N. Tahir, S. Passerini, R. Zentel and W. Tremel, *J. Mater. Chem. A*, 2016, **4**, 612–619.
29 L. Jin, Y. X. Yao, Z. Han, W. H. Bin, D. Shujiang and L. X. Wen, *Angew. Chem., Int. Ed.*, 2014, **53**, 12803–12807.
30 R. Hu, D. Chen, G. Waller, Y. Ouyang, Y. Chen, B. Zhao, B. Rainwater, C. Yang, M. Zhu and M. Liu, *Energy Environ. Sci.*, 2016, **9**, 595–603.
31 S. Y. Lee, K. Y. Park, W. S. Kim, S. Yoon, S. H. Hong, K. Kang and M. Kim, *Nano Energy*, 2016, **19**, 234–245.
32 L. Zhong, X. H. Liu, G. F. Wang, S. X. Mao and J. Y. Huang, *Phys. Rev. Lett.*, 2011, **106**, 248302.
33 M. Cao, M. Zhang, L. Xing, Q. Wang and X. Y. Xue, *J. Alloys Compd.*, 2016, **694**, 30–39.
34 X. Zhou, Z. Dai, S. Liu, J. Bao and Y. G. Guo, *Adv. Mater.*, 2014, **26**, 3943–3949.
35 X. Liu, D. Teng, T. Li, Y. Yu, X. Shao and X. Yang, *J. Power Sources*, 2014, **272**, 614–621.
36 H. Liu, R. Hu, W. Sun, M. Zeng, J. Liu, L. Yang and M. Zhu, *J. Power Sources*, 2013, **242**, 114–121.
37 B. Zhang, J. Huang and J. K. Kim, *Adv. Funct. Mater.*, 2015, **25**, 5222–5228.
38 B. Zhang, Y. Yu, Z. Huang, Y. B. He, D. Jang, W. S. Yoon, Y. W. Mai, F. Kang and J. K. Kim, *Energy Environ. Sci.*, 2012, **5**, 9895–9902.
39 W. Dong, J. Xu, C. Wang, Y. Lu, X. Liu, X. Wang, X. Yuan, Z. Wang, T. Lin, M. Sui, I. W. Chen and F. Huang, *Adv. Mater.*, 2017, **29**, 1700136.
40 S. Zhang, K. Zhao, T. Zhu and J. Li, *Prog. Mater. Sci.*, 2017, **89**, 479–521.
41 Y. Sun, N. Liu and Y. Cui, *Nat. Energy*, 2016, **1**, 16071.
42 Y. Jin, S. Li, A. Kushima, X. Zheng, Y. Sun, J. Xie, J. Sun, W. Xue, G. Zhou, J. Wu, F. Shi, R. Zhang, Z. Zhu, K. So, Y. Cui and J. Li, *Energy Environ. Sci.*, 2017, **10**, 580–592.
43 L. Zhang, Z. C. Zhang and K. Amine, in *Lithium Ion Batteries - New Developments*, ed. I. Belharouak, InTech, Rijeka, 2012, vol. 7, pp. 173–188.
44 S. Li, J. Niu, Y. C. Zhao, K. P. So, C. Wang, C. A. Wang and J. Li, *Nat. Commun.*, 2015, **6**, 7872.

